

Numerical Modeling of Low Frequency Hydro-acoustic Waves Generated By Submarine Tsunamiogenic Earthquake

Ali Abdolali^{1,2}, Claudia Cecioni², James T. Kirby¹, Paolo Sammarco³, Giorgio Bellotti², Leopoldo Franco²

¹Center for Applied Coastal Research, University of Delaware, Newark DE, USA

²Engineering Department, Roma Tre University, Rome, Italy

³Civil Engineering Department, University of Roma Tor Vergata, Rome, Italy

ABSTRACT

We investigate the role of a viscous compressible sedimentary layer underlying sea water on the formation, propagation and attenuation of hydro-acoustic waves. The analysis of low frequency pressure waves can be used for evaluation of stratified sediment structure. Two models based on depth-integration, for rigid and permeable sea bed are presented. The hydro-acoustic waves modeling, hereinafter presented can be used for tsunami prediction in large scale domains, overcoming computational difficulties of three-dimensional models and therefore enhance the promptness and accuracy of Tsunami Early Warning Systems (TEWS).

KEYWORD: Hydro-acoustic waves; Tsunami; Compressible Fluid; Viscous Sediment; Peak Frequency; Damping term

INTRODUCTION

Tsunamiogenic fast movements of the sea-bed generate pressure waves in weakly compressible sea water, namely hydro-acoustic waves, which travel at the sound celerity in water (about 1500 m/s). These waves travel much faster than the counterpart long free-surface gravity waves and contain significant information about the source (Chierici et al., 2010). Measurement of hydro-acoustic waves can therefore anticipate tsunami arrival and significantly improve the capability of tsunami early warning systems (Cecioni et al., 2014b). Inherently, hydro-acoustic waves cannot propagate upslope. Therefore, measurement should be done in the deep sea in order to avoid depth effects on arriving signals (Abdolali et al., 2014). However, applications to real cases require detailed numerical modeling in order to clearly define the time series at point A due to a source at point B. Three-dimensional models (Nosov and Kolesov, 2007) are straightforward to use, but require unrealistic computational times when applied to large-scale geographical areas, i.e. they cannot be used for a systematic investigation on an oceanic scale of prediction. To overcome computational difficulties and limits of analytical solutions, Sammarco et al. (2013) proposed a hyperbolic mild slope equation for

weakly compressible fluid on a rigid bottom. Subsequently, the model has been used to simulate hydro-acoustic wave propagation in the central and eastern Mediterranean Sea, generated by two main destructive historical earthquakes: the 365 *AD Crete* event and the 1693 *Sicily* event (Cecioni et al., 2014a; Tonini et al., 2011). The same model has been used to reproduce the 28 October 2012 7.8 *Mw* earthquake occurred off the West coast of *Haida Gwaii* archipelago, *Canada*. For this event, deep water field measurements are available for comparison (Abdolali et al., 2015a). The model results for the gravity wave (tsunami) are in good agreement with observations. While the model of hydro-acoustic wave is further complicated by the effects of compressible viscous sediment layer at the sea bottom, which have a deep influence on hydro-acoustic wave propagation over large distances (Abdolali et al., 2015b). In this paper, we summarize recent progress in the modeling of hydro-acoustic waves. We start from describing the role of sedimentary layers in formation and propagation of hydro-acoustic waves in the framework of 3D linear potential theory. Then the Mild-Slope Equation in Weakly Compressible fluid (MSEWC) for a rigid sea bed is presented, showing how its solution reduces the computational costs compared to the solution of 3D problem. The MSEWC reduces the computational problem from three to two dimensions, hence reducing dramatically the computational costs. Then, we further extend the capabilities of the model by including the effects of a sediment layer at the bottom. On the basis of the numerical results presented herein, several conclusions on the possible use of hydro-acoustic waves as support to Tsunami Early Warning Systems can be drawn.

HYDRO-ACOUSTIC WAVE MODEL

Three Dimensional Model

Consider the interaction of a train of hydro-acoustic waves in an inviscid water layer of depth $h(x, y, t)$ with the sound celerity of c and water density ρ overlying stratified viscous sediment layers of thickness $a^{(i)}(x, y, t)$, with $h_s^{(i)} = h + \sum_{n=1}^i a^{(n)}$ where $h_s^{(i)}(x, y, t)$ is the

total depth. $c_s^{(i)}$ is celerity of sound within sediment with density of $\rho_s^{(i)}$ and apparent sediment kinematic viscosity of $\nu_s^{(i)}$. g is the gravitational acceleration. The vertical coordinate, z , is measured positively upwards from the undisturbed free surface at $z = 0$, and x and y denote horizontal cartesian coordinates as shown in Fig. 1. The other parameters are for sudden displacement of source area with semi-length b and rise time τ . The transient sea bed velocity, ζ_t , with a residual displacement ζ_0 , is a trigonometric function expressed by

$$\zeta_{s,t}^{(i)} = \frac{\zeta_0}{2} \left[1 - \cos\left(\frac{2\pi(t-t_0)}{\tau}\right) \right] [H(t-t_0) - H(t-t_0-\tau)], \quad (1)$$

where $H(t)$ is the Heaviside step function. The time series of bottom displacement and velocity are shown in Fig. 2. For the case of two sedimentary layers, the linearized weakly compressible wave equations governing the fluid potential $\Phi(x, y, z, t)$ in the water layer and $Q^{(i)}(x, y, z, t)$ in the stratified viscous sediment layers, are given by

$$\begin{aligned} \Phi_{tt} - c^2 \nabla^2 \Phi &= 0; & -h + \eta_2 \leq z \leq \eta_1 \\ Q_t^{(1)} - c_s^{(1)2} \nabla^2 Q^{(1)} - 2\nu_s^{(1)} (\nabla^2 Q_t^{(1)}) &= 0; & -h_s^{(1)} + \eta_3 \leq z \leq -h + \eta_2 \\ Q_t^{(2)} - c_s^{(2)2} \nabla^2 Q^{(2)} - 2\nu_s^{(2)} (\nabla^2 Q_t^{(2)}) &= 0; & -h_s^{(2)} \leq z \leq -h_s^{(1)} + \eta_3 \end{aligned} \quad (2)$$

where ∇^2 is the Laplacian in 3D and subscripts on dependent variables denote partial derivatives. The interfacial displacements $\eta_i(x, y, t)$; $i = 1, 2, 3$, represent response of the free surface and layers interface to hydroacoustic disturbances. The apparent sediment kinematic viscosity is $\nu_s^{(i)} = \mu_s^{(i)} / \rho_s^{(i)}$. The bulk viscosity $\mu_s^{(i)}$ ranges from 10^6 up to 10^{20} Pa s (Kimura, 2006; Van Keken et al., 1993). The boundary conditions at free surface and at the bottom for two sedimentary layers are given by

$$\begin{cases} \Phi_{tt} + g\Phi_z = 0 \\ Q_z^{(2)} + \nabla_h h_s^{(2)} \cdot \nabla_h Q^{(2)} + h_{s,t}^{(2)} = 0 \end{cases} \quad \text{at } z = 0 \quad \text{at } z = -h_s^{(2)} \quad (3)$$

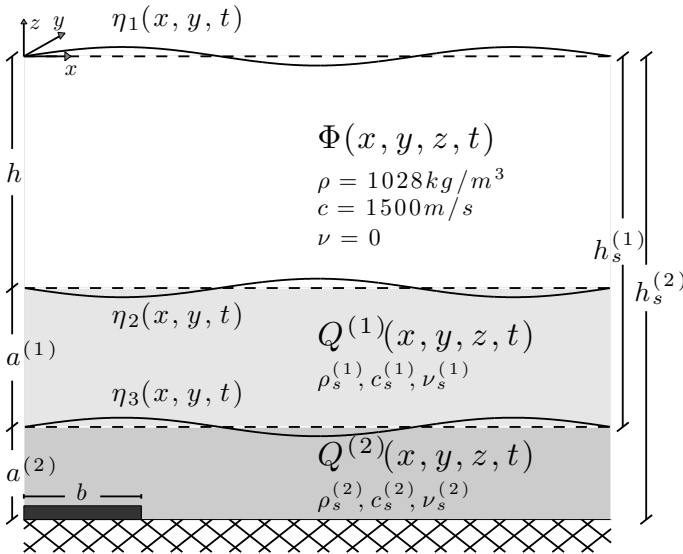


Figure 1: Schematic view of fluid domain.

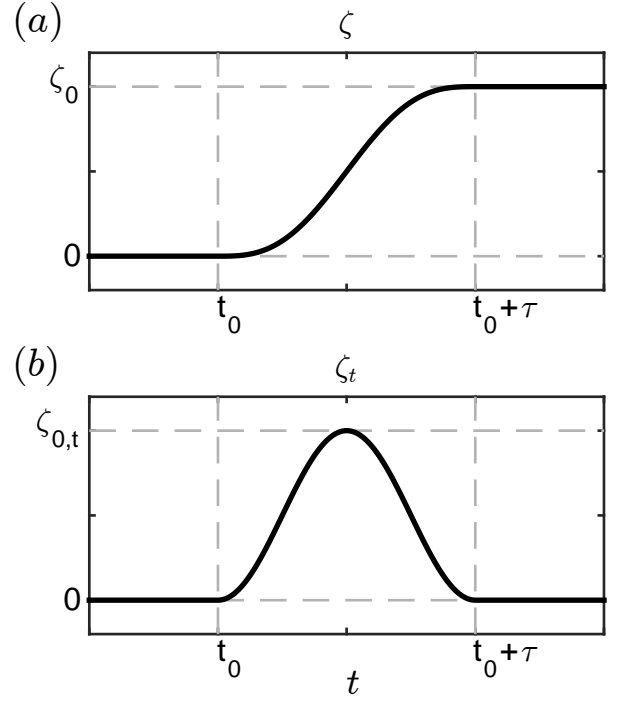


Figure 2: Rising mechanism starting at $t = t_0$ for period of τ with residual displacement of ζ_0 . (a) Bottom displacement time series. (b) bottom velocity time series.

where ∇_h is the horizontal gradient operator and $h_{s,t}^{(2)}$ is the vertical bottom velocity representing displacement of the impermeable substrate. Matching conditions at the water-sediment $z = -h + \eta_2$ and sediment-sediment interfaces $z = -h_s^{(1)} + \eta_3$ consist of continuity of pressure and kinematic constraints for each layer. After linearizing with respect to the pressure perturbation and small interface displacement, the resulting conditions are

$$\begin{cases} (R^{(1)} - 1)g\eta_2 = \Phi_t - R^{(1)}Q_t^{(1)} \\ W_w = W_s^{(1)} = (-h + \eta_2)_t \end{cases} \quad \text{at } z = -h \quad (4)$$

and

$$\begin{cases} (R^{(2)} - 1)g\eta_3 = Q_t^{(1)} - R^{(2)}Q_t^{(2)} \\ W_s^{(1)} = W_s^{(2)} = (-h_s^{(1)} + \eta_3)_t \end{cases} \quad \text{at } z = -h_s^{(1)} \quad (5)$$

where $R^{(1)} = \rho_s^{(1)} / \rho$ and $R^{(2)} = \rho_s^{(2)} / \rho_s^{(1)}$. The normal velocities at the interface inside the water column, W_w , and sedimentary layers, $W_s^{(i)}$, are given by:

$$\begin{cases} W_w = \Phi_z + \nabla_h h \cdot \nabla_h \Phi \\ W_s^{(1)} = Q_z^{(1)} + \nabla_h h \cdot \nabla_h Q^{(1)} \end{cases} \quad \text{at } z = -h \quad (6)$$

and

$$\begin{cases} W_s^{(1)} = Q_z^{(1)} + \nabla_h h_s^{(1)} \cdot \nabla_h Q^{(1)} \\ W_s^{(2)} = Q_z^{(2)} + \nabla_h h_s^{(1)} \cdot \nabla_h Q^{(2)} \end{cases} \quad \text{at } z = -h_s^{(1)} \quad (7)$$

In the absence of viscous behaviour of sea bottom, the dominant frequency range in the wave spectrum can be expressed by a discrete set of normal frequencies $f^{(n)}$ given by

$$f^{(n)} = (2n - 1) \frac{c}{4h}, \quad n = 1, 2, 3, \dots \quad (8)$$

Table 1: Sample computation parameters

Layer	Density (kg/m^3)	Sound Celerity (m/s)	Layer Thickness (m)
Water	$\rho = 1028$	$c = 1500$	$h = 2200$
Sediment ($i = 1$)	$\rho_s^{(1)} = 1850$	$c_s^{(1)} = 2000$	$a^{(1)} = 1000$
Sediment ($i = 2$)	$\rho_s^{(2)} = 2200$	$c_s^{(2)} = 2500$	$a^{(2)} = 1000$
Fault Length (km)	Start Time (s)	Duration (s)	Residual Displacement (m)
$b = 112$	$t_0 = 5$	$\tau = 2$	$\zeta_0 = 1$

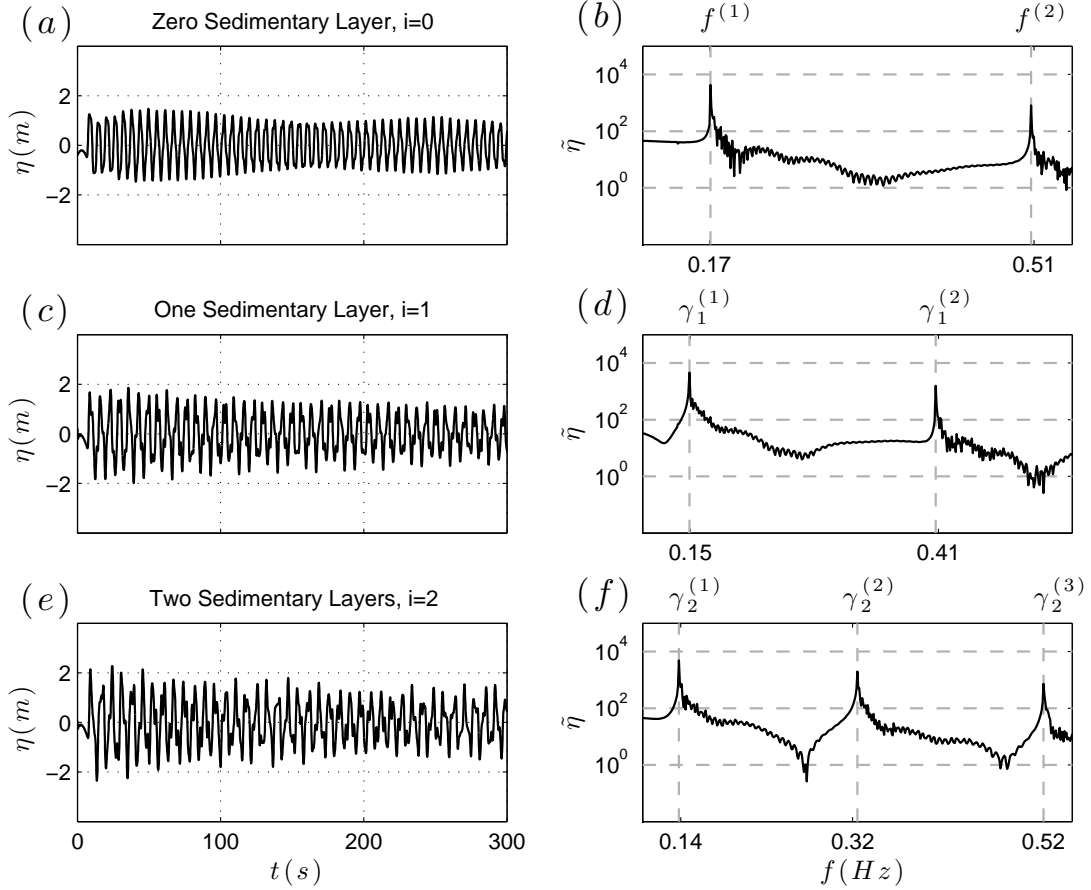


Figure 3: Results for the free surface elevation time series (left column) and their relative frequency spectra (right column) at a distance of $x = 96 km$ from epicenter, results of a sample computation carried out using a 3D flow solver with computation parameters reported in Tab. 1. Panels show the case of (a, b) no sedimentary layer, $i = 0$, compressible water model with rigid bottom; (c, d) a coupled model of compressible water and a viscous compressible sediment, $i = 1$, $\mu_s^{(1)} = 0$; (e, f) a coupled model of compressible water and two viscous compressible sedimentary layers, $i = 2$, $\mu_s^{(1,2)} = 0$. The vertical dashed lines at the right column of panels represent the peak frequencies $f^{(n)}$ calculated by Eq. (8) at panel (b), $\gamma_1^{(n)}$ calculated by Eq. (9) at panel (d) and $\gamma_2^{(n)}$ calculated by Eq. (10) at panel (f).

 Table 2: Spectral peak frequencies for $i = 0, 1, 2$ sedimentary layer(s) given by Eqs. 8, 9 and 10, relative to the first three hydro-acoustic modes

Sediment Layer(s)	1 st mode (Hz)	2 nd mode (Hz)	3 rd mode (Hz)
0 Layer	$f^{(1)} = 0.17$	$f^{(2)} = 0.51$	$f^{(3)} = 0.85$
1 Layers	$\gamma_1^{(1)} = 0.15$	$\gamma_1^{(2)} = 0.41$	$\gamma_1^{(3)} = 0.60$
2 Layers	$\gamma_2^{(1)} = 0.14$	$\gamma_2^{(2)} = 0.32$	$\gamma_2^{(3)} = 0.52$

Introducing a single underlying sediment layer ($i = 1$) acting together with water column, it lowers the spectral peak frequencies, which are determined from the following transcendent equation (Nosov et al., 2007):

$$\tan \left[\frac{2\pi\gamma_1^{(n)}h}{c} \right] \tan \left[\frac{2\pi\gamma_1^{(n)}a^{(1)}}{c_s^{(1)}} \right] = \frac{\rho_s^{(1)}c_s^{(1)}}{\rho c} \quad (9)$$

where $\gamma_1^{(n)}$ denotes the normal mode frequencies for the coupled case. Note that in the case of $a^{(1)} = 0$, the set of normal modes described by Eqs. (8) and (9) coincide. Adding a second sedimentary layer ($i = 2$), natural frequencies, $\gamma_2^{(n)}$ toward lower values further shifts according to

$$\frac{\frac{\rho_s^{(2)}c_s^{(2)}}{\rho_s^{(1)}c_s^{(1)}} - \tan \left[\frac{2\pi\gamma_2^{(n)}a^{(1)}}{c_s^{(1)}} \right] \tan \left[\frac{2\pi\gamma_2^{(n)}a^{(2)}}{c_s^{(2)}} \right]}{\tan \left[\frac{2\pi\gamma_2^{(n)}a^{(2)}}{c_s^{(2)}} \right] + \frac{\rho_s^{(2)}c_s^{(2)}}{\rho_s^{(1)}c_s^{(1)}} \tan \left[\frac{2\pi\gamma_2^{(n)}a^{(1)}}{c_s^{(1)}} \right]} = \frac{\rho c}{\rho_s^{(1)}c_s^{(1)}} \tan \left[\frac{2\pi\gamma_2^{(n)}h}{c} \right] \quad (10)$$

Note that in the case of $a^{(2)} = 0$, the set of normal modes described by Eqs. (9) and (10) coincide.

Observation during *Tokachi-Oki* 2003 event shows that the dominant peak frequencies are lower than values estimated by Eq. (8), for one single water column with rigid bottom assumption (Nosov et al., 2007). This suggests to investigate the role of sedimentary layers in formation of standing waves, developed vertically between the sea bottom and the water surface. A sample computation is carried out using a full 3D solver for three computational domains (rigid bottom/one sedimentary layer ($i = 1$)/two sedimentary layers coupled with water column ($i = 2$)). The model parameters are shown in Tab. 1. The results are depicted in Fig. 3, which shows the free surface elevation time series η (left column) and the corresponding frequency spectrum $\tilde{\eta}$ (right column) at 96 km from the epicenter. In panels (a, b) one layer of compressible water model with impermeable sea bottom is considered. The numerical spectrum and analytical calculation for natural modes expressed by Eq. (8) are essentially identical. In panels (c, d) and for the case of a sedimentary layer underlying the water column, the dominant frequencies match the roots of Eq. (9). In panels (e, f) where two sedimentary layers are coupled with water layer, the natural modes are in good agreement with values estimated by Eq. (10). The first three peak frequencies for different models are presented in Tab. 2. The comparison shows that in order to properly model the shifts in peak frequencies, it is essential to consider the underlying layers. In the following section, the effective sediment thickness is explored.

Damping Behaviour

In the framework of hydro-acoustic wave theory, the underlying sedimentary layer can be treated as a ‘‘Fluid-Like’’ medium coupled with water column at the interface (Chierici et al., 2010; Abdolali et al., 2015b). In this regard, sediment intergranular friction governs the sound propagation field leading to change in natural frequencies and evanescence of hydro-acoustic waves. A nondimensionalization of the sediment layer equation yields a parameter $\epsilon = \omega\nu_s/c_s^2$ characterizing the size of the damping term relative to the undamped wave equation. A series of computations have

been carried out to reveal to what extent the damping term ϵ can affect the damping rate and dominant peak frequencies. The water depth, sediment thickness, densities and sound speeds within water and sediment and source parameters are the same as Figure 3 with different bulk viscosities ($10^6 < \mu_s^{(1)} < 10^{20}$ Pas). As an example, the results of one simulation for $\mu_s^{(1)} = 2 \times 10^8$ Pas in term of free surface elevation at $x = 96$ km from source is shown in Fig. 4. The time series is normalized by the maximum free surface elevation. As is shown in the plot, hydro-acoustic wave amplitude decreases gradually. An exponential fitting curve (red line) is extrapolated among the blue dots representing peak amplitudes

$$\frac{\eta}{\eta_{max}} = e^{-\theta\omega t} \quad (11)$$

where θ is dimensionless damping rate. In Fig. 5, the variation of the first three peak frequencies is plotted for different damping terms ϵ . It can be seen from the plot that for small $\epsilon/\omega < 0.02$, the dominant frequencies are close to those estimated by Eq. (9) for inviscid compressible sediment case. Then, the peak frequencies increase to reach those estimated from Eq. (8) for rigid bottom case ($\epsilon/\omega > 2$). The damping rate variation is plotted in Fig. 6. Where the damping term is small ($\epsilon < 10^{-4}$), sediment acts like an inviscid fluid. In this condition, the coupled system consists of two fluids with different densities and sound speeds. As a result, the long lasting hydro-acoustic waves are not absorbed due to internal losses at grain-to-grain contacts. The damping rate increases while the damping term is rising from $\epsilon = 10^{-4}$ to 8×10^{-2} . Crossing the maximum damping rate θ , the permeability of underlying layer decreases gradually. It reaches $\epsilon > 10^2$ where model result is similar to one water column with rigid bottom.

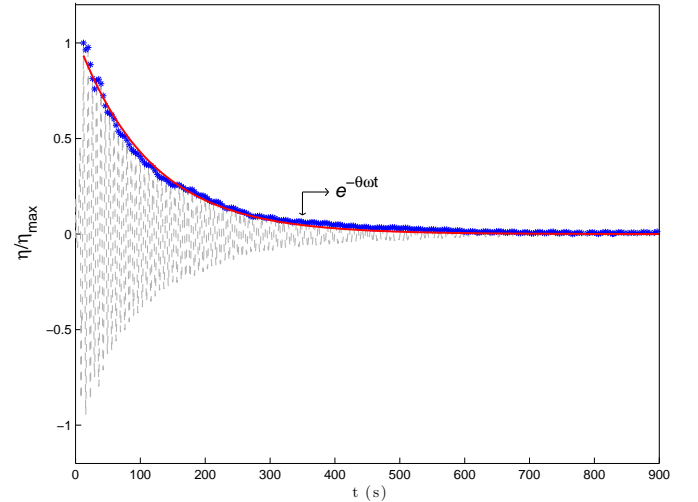


Figure 4: Time series of free surface elevation normalized by the maximum value (η/η_{max}) for the case of $h = 2200$ m water column overlying a single sedimentary layer ($a^{(1)} = 1000$ m). The other parameters are $c = 1500$ m/s, $c_s^{(1)} = 2000$ m/s, $\rho = 1028$ kg/m³, $\rho_s^{(1)} = 1850$ kg/m³ and $\mu_s^{(1)} = 2 \times 10^8$ for a unit source area with semi-length $b = 112$ km and rising time $\tau = 2$ s. Blue dots represent temporal variation of the peak amplitudes. Red line is the fitting curve representing an exponential function ($e^{-\theta\omega t}$).

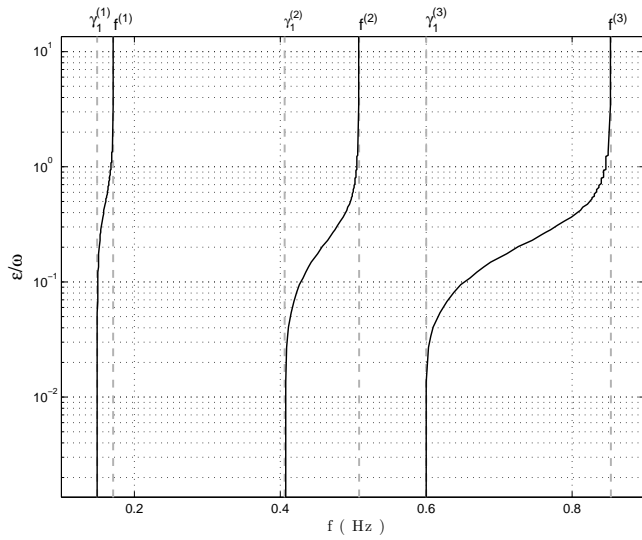


Figure 5: Variation of peak frequencies for different damping term (ϵ). The light gray dashed lines represent the natural modes for rigid bottom $f^{(n)}$ and two layered system $\gamma_1^{(n)}$ shown in Tab.2.

Overall, taking the damping term into account leads to temporal damping of hydro-acoustic waves. In addition, depending on the damping term magnitude, it can change the dominant peak frequencies. From a practical point of view, the analysis of measured time series during tsunamigenic events reveals the sedimentary layer characteristics and justify the mismatch between one layer/multi-layers assumptions. It can be used to optimize the number of sedimentary layers which should be considered for numerical modeling of hydro-acoustic wave fields. The accurate thickness, density and sound speed within stratified sedimentary layers, taken from presented analysis, improve the accuracy of model results.

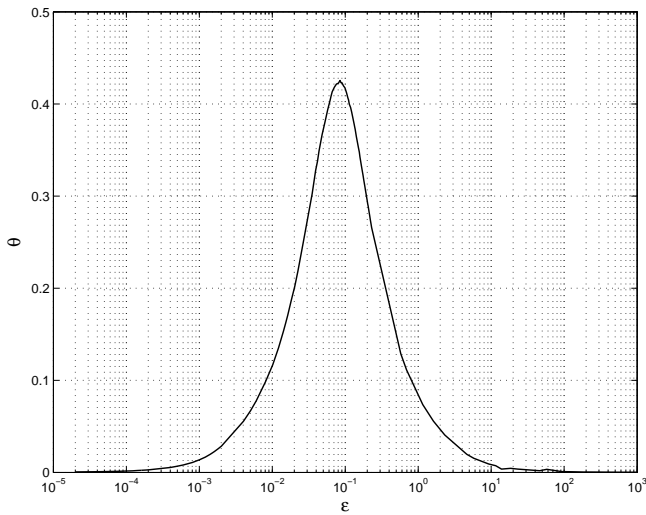


Figure 6: Variation of dimensionless damping rate θ as is shown in Fig. 4 for different damping terms ϵ .

Depth Integrated Model for rigid bottom

Assuming a rigid bottom ($a^{(i)} = 0$; $h_s = h$), Sammarco et al. (2013) developed a Mild-Slope Equation in Weakly Compressible fluid (MSEWC), via a proper application of the averaging technique to the problem (2), for the case of constant c and mild sloped sea-bed ($\nabla h \ll kh$)

$$\psi_{n_n} \left(\frac{C_n}{c_s^2} + \frac{1}{g} \right) - \nabla (C_n \nabla \psi_n) + \left(\frac{\omega^2}{g} - \beta_n^2 C_n \right) \psi_n = h \mu D_n \quad (12)$$

where $\psi(x, y, t)$ is the fluid velocity potential at the undisturbed free-surface. The subscript n indicates that Eq. (12) is valid for the generic n^{th} mode (hydro-acoustic and gravity). Superimposition of the solutions of Eq. (12) for each mode will lead to complete modeling of the fluid potential, $\Phi(x, y, z, t) = \sum_{n=0}^{\infty} \psi_n(x, y, t) f_n(z)$, generated by a fast sea-bed motion, where the f_n 's are the classic eigenfunctions of the constant depth homogeneous problem

$$f_n(z) = \frac{\cosh[\beta_n(h+z)]}{\cosh(\beta_n h)}. \quad (13)$$

In Eq. (12) β_n 's are the roots of the dispersion relation

$$\beta_n = \begin{cases} n=0 & \beta_n = \beta_0 & \omega^2 = g\beta_0 \tanh(\beta_0 h) \\ n \geq 1 & \beta_n = i\tilde{\beta}_n & \omega^2 = -g\tilde{\beta}_n \tan(\tilde{\beta}_n h) \end{cases} \quad (14)$$

while the terms $C_n(x, y)$ and $D_n(x, y)$ are given by

$$C_n(x, y) = \int_{-h}^0 f_n^2 dz = \frac{2\beta_n h + \sinh(2\beta_n h)}{4\beta_n \cosh^2(\beta_n h)} \quad (15)$$

$$D_n(x, y) = \frac{1}{\cosh^2(\beta_n h)} \frac{\int_{-h}^0 f_n dz}{\int_{-h}^0 f_n^2 dz} = \frac{4 \tanh(\beta_n h)}{(2\beta_n h + \sinh(2\beta_n h))}. \quad (16)$$

More details on the derivation can be found in Sammarco et al. (2013). In the time domain the MSEWC reproduces the fluid potential characteristic of a narrow frequency banded wave spectrum, around the value of a carrier frequency, which is used for the computation of β_n , C_n and D_n . For each narrow frequency band of the wave spectrum, Eq. (12) is solved and then the results are superimposed.

A sample computation has been carried out to verify whether the model equation (12) can be safely applied in place of a more computationally expensive 3D treatment. We present results for a vertical section in x, z through laterally uniform domains with no y -dependence, with a constant water depth. Frequency bands of width $\Delta f = 0.02$ Hz have been selected to discretize the forcing spectrum. The time step is $t = 0.1$ s. The numerical solvers are applied on a computational domain 200 km long; given the symmetry of the problem about the middle of the earthquake ($x = 0$), computations are undertaken only for half of the physical domain. The Sommerfeld radiation condition is applied at the open end of the domain, so that the waves leave the domain freely. At $x = 0$, a fully reflective boundary condition is used in order to preserve symmetry. The results are presented in the Fig. 7 in terms of free surface elevation η (left column) and corresponding

spectrum $\tilde{\eta}$ (right column) at two virtual surface gauges at $x = 50$ and 100 km. Semi-fault length and water depth are $b = 15$ km and $h = 2200$ m respectively. The maximum mesh size is 200 m, for a total of 750 elements in the case of depth-integrated model (12), and 25000 triangular elements for 3D one (2). The computational time to reproduce 1000 s of real-time simulation was about 10 minutes for (12) and about 2 hours for (2) on a computer equipped with an *i7* 3.2 GHz CPU and 64 GB RAM. The time series of three dimensional (light gray) and depth integrated models are identical in terms of modulation, amplitude and arrival time. The frequency spectra are in good agreement dominant by first cut off frequency calculated by Eq. (8).

Depth Integrated Model for water column coupling with single sedimentary layer

Considering underlying sedimentary layer ($a^{(2)} = 0$, $h_s = h + a^{(1)}$), in the hypothesis of constant sound c and $c_s^{(1)}$, the upper and lower layer potentials may be expressed according to $\Phi(x, y, z, t) =$

$\sum_{n=0}^{\infty} \psi_n(x, y, t) M_n(z)$ and $Q^{(1)}(x, y, z, t) = \sum_{n=0}^{\infty} \psi_n(x, y, t) N_n(z)$ respectively. The eigenfunctions $M_n(z)$ and $N_n(z)$ for the upper and lower layers are given by

$$M_n = \frac{(1 - \lambda_n T_n) \cosh(\beta_{w,n}(h+z)) + (\lambda_n - T_n) \sinh(\beta_{w,n}(h+z))}{(1 - \lambda_n T_n) \cosh(\beta_{w,n}h) + (\lambda_n - T_n) \sinh(\beta_{w,n}h)} \quad (17)$$

$N_n =$

$$\frac{(\lambda_n - T_n) \cosh \beta_{s,n}(h_s + z)}{\alpha_n \sinh(\beta_{s,n}a^{(1)}) [(1 - \lambda_n T_n) \cosh(\beta_{w,n}h) + (\lambda_n - T_n) \sinh(\beta_{w,n}h)]} \quad (18)$$

where $T_n = \tanh(\beta_{w,n}h)$, $\lambda_n = \omega^2/g\beta_{w,n}$ and $\alpha_n = \beta_{s,n}/\beta_{w,n}$. The separation constants $\beta_{w,n}$ and $\beta_{s,n}$ for water and sediment layers respectively are given by

$$\beta_{w,n}^2 = k_n^2 - \left(\frac{\omega}{c}\right)^2; \quad \beta_{s,n}^2 = k_n^2 - \left(\frac{\omega}{c_s^{(1)}}\right)^2 \quad (19)$$

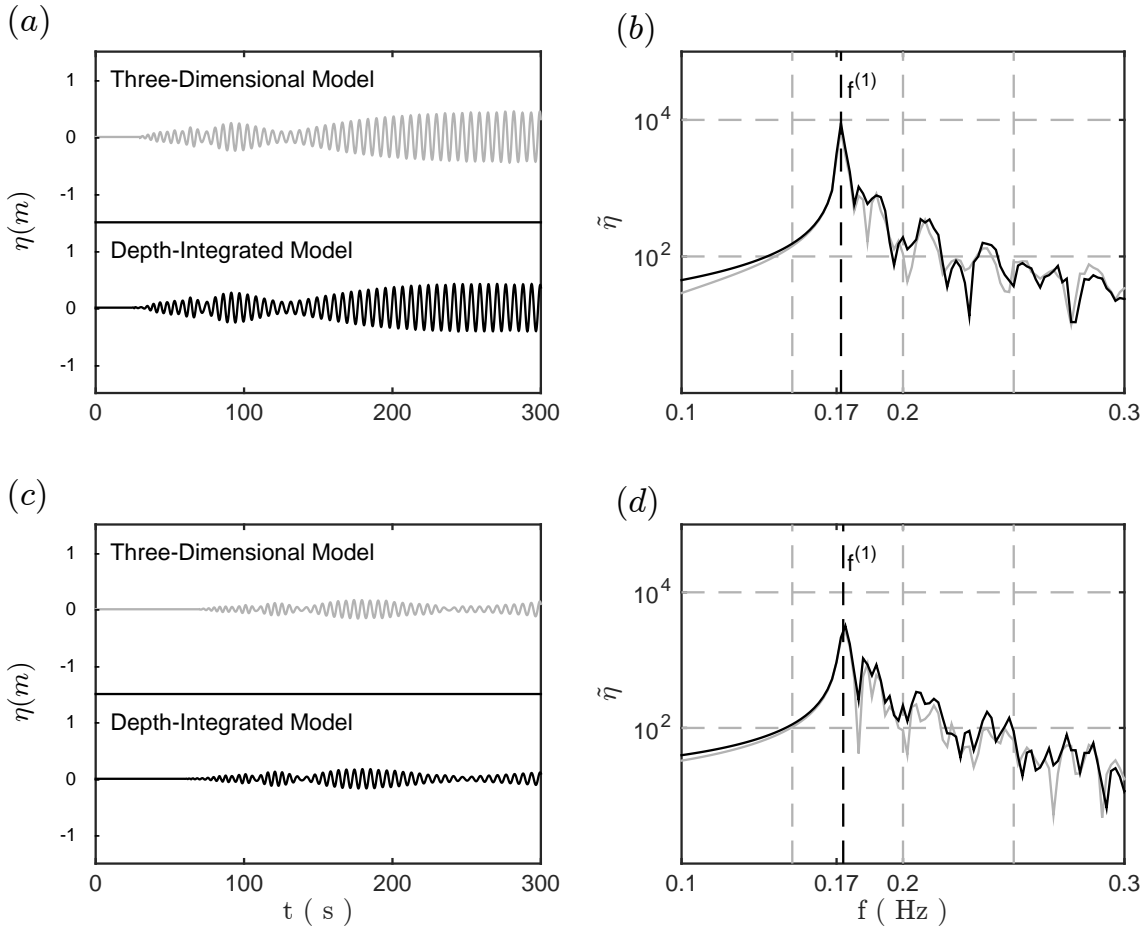


Figure 7: Results for the free surface elevation time series (left column) and their relative frequency spectra (right column) at a distance of $x = 50$ km (a, b) and $x = 100$ km from epicenter (c, d), results of a sample computation carried out using a 3D model (light gray) and depth integrated (black) model (MSEWC) in a constant depth with impermeable bottom, $h = 2200$ m, $c = 1500$ m/s, $\rho = 1028$ kg/m³ for a unit source area with semi-length $b = 15$ km and rising time $\tau = 2$ s. The vertical dashed lines represents the frequency peaks $f^{(n)}$ calculated by Eqs. (8)

where k_n is the wave number. The dispersion relation for $\beta_{w,n}$ and $\beta_{s,n}$ is given by

$$\lambda_n^2(R^{(1)} + \alpha_n T_n \hat{T}_n) - \lambda_n R^{(1)}(T_n + \alpha_n \hat{T}_n) + (R^{(1)} - 1)\alpha_n T_n \hat{T}_n = 0 \quad (20)$$

where $\hat{T}_n = \tanh(\beta_{s,n} a^{(1)})$. Eq. (20) is a quartic system in ω describing a doubly-infinite set of surface waves (with horizontal displacements in phase at the layer interface) and internal waves (with horizontal displacements 180° out of phase). By a proper use of the averaging technique to the problem (2), taking the advantage of orthogonality within the spatial derivative terms, and making use of the interfacial kinematic and dynamic boundary conditions, Abdolali et al. (2015b) found a hyperbolic mild slope equation for weakly compressible fluid overlying a sediment viscous layer, MSWDWC in the following form

$$(I_2^m \psi_{m,t})_t - \nabla_h \cdot [I_1^m \nabla_h \psi_m] + [\omega^2 I_2^m - k_m^2 I_1^m] \psi_m + 2R^{(1)} \epsilon \frac{\omega}{c_s^{(1)2}} K_n \psi_{m,t} = D_1^m h_t + D_2^m h_{s,t}, \quad (21)$$

Model coefficients are given by

$$I_1^m = I_{mm} + R^{(1)} K_{mm} \quad (22)$$

$$I_2^m = \frac{I_{mm}}{c^2} + R^{(1)} \frac{K_{mm}}{c_s^{(1)2}} + \frac{1}{g} \quad (23)$$

$$D_1^m = -[M_m(-h) - R^{(1)} N_m(-h)] \quad (24)$$

$$D_2^m = -R^{(1)} N_m(-h_s), \quad (25)$$

where $I_{mm}(x, y, t)$ and $K_{mm}(x, y, t)$ are given by

$$I_{mm} = \int_{-h}^0 M_m^2 dz = \frac{h}{2G_1^m} [(1 - 2\lambda_m T_m + \lambda_m^2) + (1 - \lambda_m^2) G_1^m] \quad (26)$$

$$K_{mm} = \int_{-h_s}^{-h} N_m^2 dz = \frac{h(\lambda_m - T_m)^2}{2\alpha_m^3 T_m \hat{T}_m} \frac{1 + G_2^m}{G_1^m} \quad (27)$$

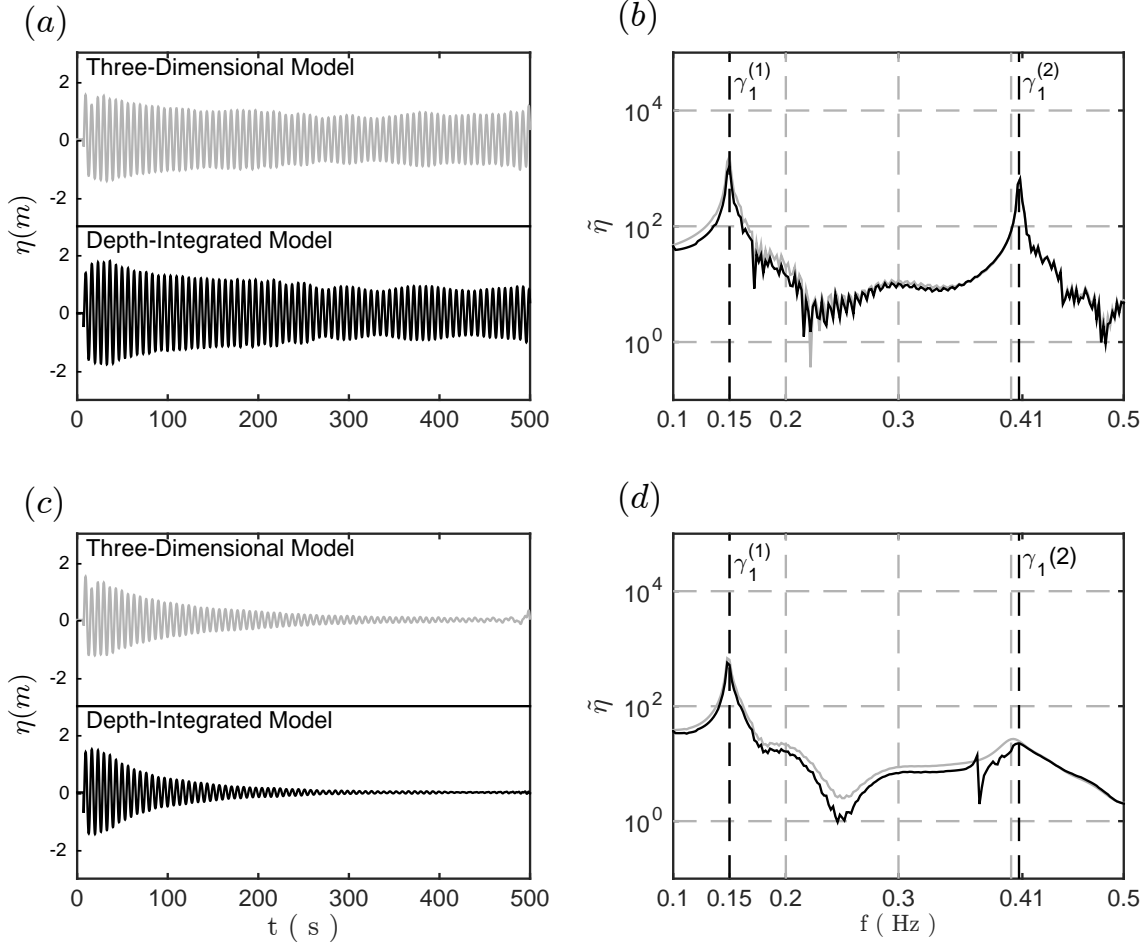


Figure 8: Results for the free surface elevation time series at 96 km from tsunamigenic source from 3D (light gray) and depth integrated (black) models in a constant depth, $h = 2200$ m, $a^{(1)} = 1000$ m, $c = 1500$ m/s, $c_s^{(1)} = 2000$ m/s, $\rho = 1028$ kg/m³, $\rho_s = 1850$ kg/m³, for a unit source area with semi-length $b = 112$ km and rising time $\tau = 1$ s. (a, b) Time series and corresponding spectra of free surface elevation where $\mu_s^{(1)} = 0$ and (c, d) $\mu_s^{(1)} = 2 \times 10^8$ Pa s with $\gamma_1^{(1)} = 0.15$ and $\gamma_1^{(2)} = 0.41$ Hz.

with

$$G_1^m = \frac{2\beta_{w,m}h}{\sinh(2\beta_{w,m}h)} \quad (28)$$

$$G_2^m = \frac{2\beta_{s,m}a^{(1)}}{\sinh(2\beta_{s,m}a^{(1)})} \quad (29)$$

More details on the derivation can be found in Abdolali et al. (2015b). For specific conditions the Eq. (21) gives the same solution as that previously proposed by Sammarco et al. (2013), i.e. $R^{(1)} = 1$ or $a = 0$ or $\epsilon \gg 1$. To verify the depth-integrated model, a sample computation has been done for constant depths, solving both the 3D problem and Eq. (21). The time step and the discretization of the spectra are the same of the (12). The computational time to reproduce 1000 s of real-time simulation was about 10 minutes for (21) and about 3 hours for (2), using the same computer of the previous simulation. The results are presented in the Fig. 8 in terms of free surface elevation η and corresponding spectrum $\tilde{\eta}$. Results are shown for a virtual surface gauge at $x = 96$ km over a 112 km semi-fault where water depth

and sediment thickness are $h = 2200$ and $a^{(1)} = 1000$ m respectively. In panel (a, b) the results are related to the case of inviscid sediment. The 3D model (light gray) and depth integrated model (black) are in optimal agreement. The peak frequencies are at $\gamma_1^{(1)} = 0.15$ and $\gamma_1^{(2)} = 0.41$ Hz, corresponding to the first and second cut off frequencies for coupled system defined by Eq. (9). The hydro-acoustic waves remain at the same order of the generated ones until the end of computations. In lower panels (c, d), we add the dissipation term into the equation ($\mu_s^{(1)} = 2 \times 10^8$ Pa s) leading to temporal absorption of hydro-acoustic waves.

In order to check the depth-integrated model performance for varying sea bottom and large bulk viscosity of sediment against fully 3D model, a sample computation is carried out. The domain's geometry, depicted in the upper plot of Fig. 9, has a 200 km area with water depth of respectively 2 and 3.5 km in left and right side of domain and an sloping area of 50 km in the middle. The sediment thickness is constant and equal to 1 km. The earthquake occurs in the shallower area (2 km water depth). It has a width of 15 km and moves vertically with a bottom velocity shown in Fig. 2 for a total displacement of $\zeta_0 = 1$ m given by (1).

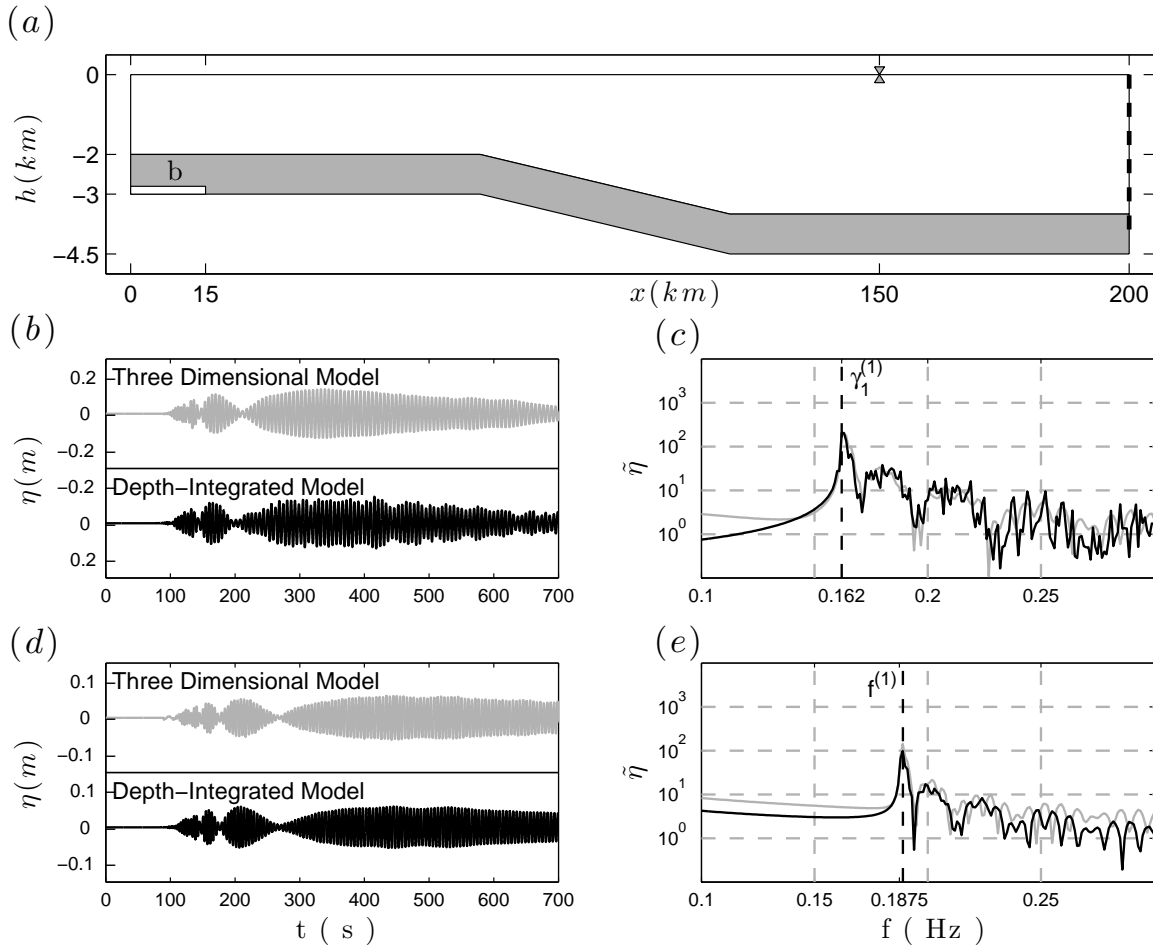


Figure 9: The case of varying sea bottom and sediment thickness with tsunamigenic source at shallower part. (a) The computational domain. Results for the free surface elevation time series at 150 km from tsunamigenic source from 3D (light gray) and depth integrated models MSEDWC (black), $c = 1500$ m/s, $c_s^{(1)} = 2000$ m/s, $\rho = 1028$ kg/m³, $\rho_s^{(1)} = 1850$ kg/m³ for a unit source area with semi-length $b = 15$ km and rising time $\tau = 1$ s. (b, c) Results for coupled model with $\mu_s^{(1)} = 0$ and (d, e) for $\mu_s^{(1)} = 10^{15}$ Pa s.

The results are presented in Fig. 9 in terms of time series of free surface elevation η and corresponding spectra $\tilde{\eta}$, at a distance $x = 150 \text{ km}$ from the moving sea bed area. The two time series are in good agreement, both in terms of amplitude and modulation of the signal. The comparison results show that the peak frequency shifts from $\gamma_1^{(1)} = 0.162 \text{ Hz}$ for $\mu_s^{(1)} = 0$ to $\gamma_1^{(1)} = f^{(1)} = 0.1875 \text{ Hz}$ for $\mu_s^{(1)} = 10^{15} \text{ Pa s}$.

CONCLUSION

Considering the stratified sedimentary layers in numerical modeling of hydro-acoustic waves can improve the accuracy of model result. The permeable sea bottom causes hydro-acoustic wave attenuation and leads to a shift in dominant peak frequencies. However, due to existence of uncertainties about sediment structure in real ocean with variable-water/sediment depth, a careful analysis is needed to optimize the number of layers required to obtain reasonable results and choose appropriate density and sound speed of each layer. In this regard, a series of computations have been carried out to extract the range of effective sediment characteristics on hydro-acoustic wave field. It can be used in the analysis of measured time series during past tsunamigenic events and used in future modeling.

In addition, a numerical model able to consider a weakly compressible inviscid fluid coupled with a compressible viscous sedimentary layer in which waves are generated by a moving bottom and then propagate over a mildly sloped sea bed is derived (Mild Slope Equation for Dispersive Weakly Compressible fluids, MSEDWC). Solution of the equation allows the description of all the mechanics in the x, y plane, overcoming at the same time both analytical and numerical difficulties. Indeed on the one hand, by expanding in series of the vertical eigenfunctions, the MSEDWC can be applied to more complex geometries other than the horizontal or piecewise horizontal in the x, z vertical plane as in the seminal work of Chierici et al. (2010) and Eyov et al. (2013). Because computational time is one order of magnitude smaller than for a fully numerical 3D model, systematic applications supporting a TEWS in the Oceans and Sea of geophysical interest will be viable.

ACKNOWLEDGEMENTS

This work was carried out under research project FIRB 2008-FUTURO IN RICERCA (“Design, construction and operation of the Submarine Multidisciplinary Observatory experiment”), Italian Ministry for University and Scientific Research (MIUR). J. T. Kirby acknowledges the support of the National Tsunami Hazard Mitigation Program, NOAA, grant NA13NWS4670014.

REFERENCES

Abdolali, A., Cecioni, C., Bellotti, G., and Kirby, J. T. (2015a). Hydro-acoustic and tsunami waves generated by the 2012 Haida Gwaii earthquake: modeling and in-situ measurements. *J. Geophys. Res.: Oceans*, In Press.

Abdolali, A., Cecioni, C., Bellotti, G., and Sammarco, P. (2014). A depth-integrated equation for large scale modeling of tsunami in weakly compressible fluid. *Coastal Engineering Proceedings*, 1(34).

Abdolali, A., Kirby, J. T., and Bellotti, G. (2015b). Depth-integrated equation for hydro-acoustic waves with bottom damping. *Journal of Fluid Mechanics*, In Press.

Cecioni, C., Abdolali, A., Bellotti, G., and Sammarco, P. (2014a). Large-scale numerical modeling of hydro-acoustic waves generated by tsunamigenic earthquakes. *Natural Hazards and Earth System Sciences Discussions*, 2(7):4629–4658.

Cecioni, C., Bellotti, G., Romano, A., Abdolali, A., Sammarco, P., and Franco, L. (2014b). Tsunami early warning system based on real-time measurements of hydro-acoustic waves. *Procedia Engineering*, 70(0):311 – 320. 12th International Conference on Computing and Control for the Water Industry, {CCWI2013}.

Chierici, F., Pignagnoli, L., and Embriaco, D. (2010). Modeling of the hydroacoustic signal and tsunami wave generated by seafloor motion including a porous seabed. *Journal of Geophysical Research*, 115(C03015).

Eyov, E., Klar, A., Kadri, U., and Stiassnie, M. (2013). Progressive waves in a compressible-ocean with an elastic bottom. *Wave Motion*, 50(5):929 – 939.

Kimura, M. (2006). Shear wave velocity in marine sediment. *Japanese journal of applied physics*, 45(5S):4824.

Nosov, M. and Kolesov, S. (2007). Elastic oscillations of water column in the 2003 tokachi-oki tsunami source: in-situ measurements and 3-d numerical modelling. *Natural Hazards and Earth System Science*, 7(2):243–249.

Nosov, M., Kolesov, S., Denisova, A., Alekseev, A., and Levin, B. (2007). On the near-bottom pressure variations in the region of the 2003 tokachi-oki tsunami source. *Oceanology*, 47(1):26–32.

Sammarco, P., Cecioni, C., Bellotti, G., and Abdolali, A. (2013). Depth-integrated equation for large-scale modelling of low-frequency hydroacoustic waves. *Journal of Fluid Mechanics*, 722:R6.

Tonini, R., Armigliato, A., Pagnoni, G., Zaniboni, F., and Tinti, S. (2011). Tsunami hazard for the city of catania, eastern sicily, italy, assessed by means of worst-case credible tsunami scenario analysis (wctsa). *Natural Hazards and Earth System Sciences*, 11:1217–1232.

Van Keken, P., Spiers, C., Van den Berg, A., and Muzyert, E. (1993). The effective viscosity of rocksalt: implementation of steady-state creep laws in numerical models of salt diapirism. *Tectonophysics*, 225(4):457–476.